

High-Fidelity Multidisciplinary Design Optimization of Aerostructural Wing Shape for Regional Jet

Kazuhiisa Chiba^{*}, Shigeru Obayashi[†] and Kazuhiro Nakahashi[‡]
Tohoku University, Sendai 980-8577, Japan

Hiroyuki Morino[§]
Mitsubishi Heavy Industries, Ltd., Nagoya 455-8515, Japan

A large-scale, real-world application of Evolutionary Multi-Objective Optimization is reported. The Multidisciplinary Design Optimization among aerodynamics, structures, and aeroelasticity of the wing of a transonic regional jet aircraft was performed using high-fidelity evaluation models. Euler and Navier-Stokes solvers were employed for aerodynamic evaluation. The commercial software NASTRAN was coupled with a Computational Fluid Dynamics solver for the structural and aeroelastic evaluations. Adaptive Range Multi-Objective Genetic Algorithm was employed as an optimizer. The objective functions were minimizations of block fuel and maximum takeoff weight in addition to drag divergence between transonic and subsonic flight conditions. As a result, nine non-dominated solutions were generated and used for tradeoff analysis among three objectives. Moreover, all solutions evaluated during the evolution were analyzed using a Self-Organizing Map as a Data Mining technique to extract key features of the design space. One of the key features found by Data Mining was the non-gull wing geometry, although the present MDO results showed the reverse-gull wings as non-dominated solutions. When this knowledge was applied to one optimum solution, the resulting design was found to have better performance and to achieve 3.6 percent improvement in the block fuel compared to the original geometry designed in the conventional manner.

I. Introduction

RECENT studies on Multidisciplinary Design Optimization (MDO) have been conducted for aircraft design^{1,2}. Pure aerodynamic optimization shows wings with a low thickness-to-chord ratio and a high aspect ratio. These wings suffer undesirable aeroelastic phenomena due to their low bending and torsional stiffness. Aerostructural interactive optimization is needed to overcome these phenomena and to allow realistic aircraft design³. This multi-objective optimization will provide a good field for application of Evolutionary Multi-Objective Optimization (EMO).

In Japan, a five year R&D project has been in progress toward the development of an environmentally friendly high performance small jet aircraft under the auspice from New Energy and Industrial Technology Development Organization (NEDO) since 2003, in which new technical features have been investigated including advanced aerodynamics, new materials, and human centered cockpit by industry-government-university cooperation.

The objective of this study is to optimize the three-dimensional wing shape for the proposed regional jet aircraft using evolutionary multi-objective optimization with high-fidelity simulations as collaboration between the Institute of Fluid Science (IFS), Tohoku University, and MHI. From the optimization results, tradeoff analysis was performed among the three objectives. Moreover, by using a data mining technique, aerostructural design knowledge for transonic regional jet aircraft has been obtained.

^{*}Graduate Student, Department of Aeronautics and Space Engineering; currently Project Researcher, Institute of Space Technology and Aeronautics, Japan Aerospace Exploration Agency. Member AIAA.

[†]Professor, Institute of Fluid Science. Associate Fellow AIAA.

[‡]Professor, Department of Aeronautics and Space Engineering. Associate Fellow AIAA.

[§]Research Engineer, Nagoya Aerospace Systems.

Copyright © 2005 by the American Institute of Aeronautics and Astronautics, Inc. All rights reserved.

In the present study, high-fidelity simulation tools, such as Reynolds-averaged Navier-Stokes (N-S) solver for aerodynamics, NASTRAN, versatile and high-fidelity commercial software, for structures and aeroelasticity were coupled together for MDO. Although the Euler/N-S solver may still be too expensive for real-world design environments, it can predict complex and nonlinear flow phenomena, such as shock wave and separation, with a high degree of accuracy. Such nonlinearity will provide a severe test case for EMO. Aided by the rapid progress in computer hardware, the demonstration described here will become standard design practice in the near future.

II. Multidisciplinary Design Optimization

A. Objective Functions

In this system, minimization of the block fuel at a required target range derived from aerodynamics and structures was selected as an objective function. In addition, two more objective functions were considered — minimization of the maximum takeoff weight and minimization of the difference in the drag coefficient between two Mach numbers, which are cruise Mach and target Maximum Operating Mach number (MMO), to prevent decrease MMO.

B. Geometry Definition

First, the planform was given by MHI. The front and rear spar positions were fixed in the structural shape based on the initial aerodynamic geometry. The wing structural model was substituted with shell elements.

The design variables were related to airfoil, twist, and wing dihedral. The airfoil was defined at three spanwise cross-sections using the modified PARSEC⁴ with nine design variables (x_{up} , z_{up} , $z_{xx_{up}}$, x_{lo} , z_{lo} , $z_{xx_{lo}}$, α_{TE} , β_{TE} , and $r_{LE_{lo}}/r_{LE_{up}}$) per cross-section as shown in Fig. 1. The twists were defined at six spanwise locations, and then wing dihedrals were defined at kink and tip locations. The twist center was set on the trailing edge in the present study. The entire wing shape was thus defined using 35 design variables. The detail of design variables is summarized in Table 1. In the present study, the geometry of each individual was generated by the unstructured dynamic mesh method^{5,6} using displacement from the initial geometry.

Table 1. Detail of design variables.

<i>serial number</i>		<i>correspondent design variable</i>
1 to 9	PARSEC airfoil	35.0% semispan location ($x_{up}, z_{up}, z_{xx_{up}}, x_{lo}, z_{lo}, z_{xx_{lo}}, \alpha_{TE}, \beta_{TE}, r_{LE_{lo}}/r_{LE_{up}}$)
10 to 18	PARSEC airfoil	55.5% semispan location
19 to 27	PARSEC airfoil	77.5% semispan location
28 to 33	Twist angle	19.3%, 27.2%, 35.0%, 55.5%, 77.5%, 96.0%
34, 35	Dihedral	35.0%, 96.0%

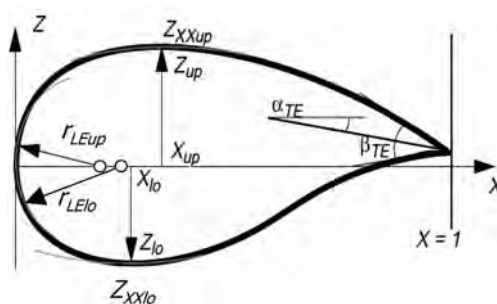


Figure 1. Illustration of the modified PARSEC airfoil shape defined by nine design variables.

C. Constraints

The five constraints were considered in the optimizer. The first three were geometrical constraints, while the last two were constraints for flight condition as follows:

1. The distribution of the parameter Δy to describe leading-edge geometry was constrained in the spanwise direction to prevent abrupt stall characteristics. Here, Δy denotes an airfoil upper surface ordinate at 6% chord from the leading edge minus the ordinate at 0.15% chord.
2. Rear spar heights were greater than required for housing of the control surfaces.
3. The lower and upper surfaces of the spars changed monotonically in the spanwise direction.
4. The lift coefficients increased monotonically with increasing Mach number to satisfy target MLD (Lift Divergence Mach number).
5. The evaluated fuel for the given range was less than the wing fuel volume.

D. Optimizer

Evolutionary algorithms (EAs), in particular genetic algorithms (GAs), are based on the theory of evolution, where a biological population evolves over generations to adapt to an environment by selection, crossover, and mutation. Fitness, individuals, and genes in the evolutionary theory correspond to the objective function, design candidates, and design variables in design optimization problems, respectively.

GAs search for optima from multiple points in the design space simultaneously and stochastically. GAs can prevent the search from settling in a local optimum. Moreover, GAs do not require computing gradients of the objective function. These features lead to the following advantages of GAs coupled with CFD: 1) GAs have the capability of finding global optimal solutions. 2) GAs can be processed in parallel. 3) High-fidelity CFD codes can be adapted to GAs easily without any modification. 4) GAs are not sensitive to any noise that might be present in the computation.

Adaptive Range Multi-Objective Genetic Algorithm (ARMOGA)⁷ is an efficient multi-objective evolutionary algorithm (MOEA) designed for aerodynamic optimization and multidisciplinary design optimization problems using high-fidelity CFD solvers with large computational time. ARMOGA has range adaptation based on population statistics, and thus the population is re-initialized every N generations so that the search region adapts toward more promising regions. Because of the re-initialization, ARMOGA can be used with a small population size similar to Micro-GA⁸. ARMOGA can be used to obtain the non-dominated solutions efficiently because of the concentrated search of the probable design space, while keeping diversity.

In the present ARMOGA, the fitness value of each solution is determined by Fleming and Fonseca's Pareto-ranking method coupled with the fitness sharing approach⁹. Each individual is assigned a rank according to the number of individuals dominating it. The assigned fitness values are divided by the niche count, which is calculated by summing the sharing function values. To find the Pareto solutions more effectively, the so-called best- N selection¹⁰ is also implemented. After determination of shared fitness values for all individuals, the Stochastic Universal Selection (SUS)¹¹ is applied to select better solutions for producing a new generation. Blended crossover (BLX- α)¹² and polynomial mutation methods¹³ are adopted for crossover and mutation.

E. Evaluation Method

The optimizer generates eight individuals per generation⁸, and evaluates aerodynamic and structural properties of each design candidate as follows:

1. Structural optimization is performed to Jig shape to realize minimum wing weight with constraints of strength and flutter requirements using NASTRAN. And then, weights of wing box and carried fuel are calculated.
2. Static aeroelastic analysis is performed at three flight conditions to determine the aeroelastic deformed shapes (1G shape) using the Euler solver and NASTRAN.
3. Aerodynamic evaluations are performed for the 1G shapes using the Navier-Stokes solver.

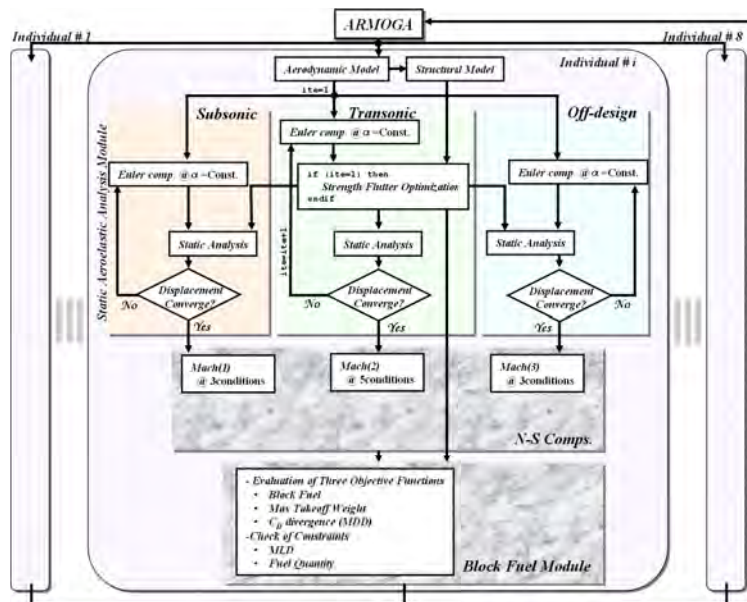


Figure 2. Flowchart of the present MDO system.

4. Flight envelope analysis is performed using the properties obtained as above to evaluate the objective functions. Using the objective functions, the optimizer generates new individuals for the next generation *via* genetic operations, such as selection, crossover, and mutation.

The conceptual flowchart for the present MDO system is shown in Fig. 2. In the present study, MSC. NASTRAN^{TM14} which is a high-fidelity commercial software is employed for the structural and aeroelastic evaluations. Besides, the in-house unstructured mesh solver named as TAS-Code (Tohoku university Aerodynamic Simulation code)^{15,16} is used to evaluate aerodynamic performance using Euler and Navier-Stokes equations.

1. Structural Optimization

In the present MDO system, structural optimization of a wing box is performed to realize minimum weight with constraints of strength and flutter requirements. Given the wing outer mold line for each individual, the finite element model of wing box is generated automatically by the FEM generator for the structural optimization. The wing box model mainly consists of shell elements representing skin, spar and rib, and other wing components, such as control surfaces and subsystems, *etc.*, are modeled using concentrated mass element. In the present structural optimization, strength and flutter characteristics are evaluated using MSC. NASTRAN.

For the strength evaluation, the static load is calculated from the pressure distribuion on the wing, which is computed by the Euler solver, assuming the 4.5G upgust condition, and then static analysis is conducted where the static load acts on the wing box structure to obtain the stress on each element. For the flutter evaluation, doublet-lattice method is used to compute the unsteady aerodynamic forces on the wing and $p-k$ method is employed as a flutter solution to obtain the critical flutter velocity.

The present structural optimization is based on the following optimality criteria:

- For strength optimization

$$\frac{\sigma_i}{F_i} = \text{Const.} \quad (1)$$

- For flutter optimization

$$\frac{\partial V_F}{\partial t_i} = \text{Const.} \quad (2)$$

where σ_i denotes the stress for i -th element, F is the allowable stress and V_F is the flutter velocity. In the structural optimization, thickness of shell elements is resized iteratively until the weight change is converged sufficiently under the strength and flutter constraints. The resizing formula is as follows:

- Strength optimization

$$t_i^{\text{new}} = \frac{t_i^{\text{old}}}{(\gamma_{\min})_i} \quad (3)$$

- Flutter optimization

$$t_i^{\text{new}} = t_i^{\text{old}} \cdot \sqrt{\frac{\frac{\partial V_F}{\partial t_i}}{\left(\frac{\partial V_F}{\partial t_i}\right)_{\text{target}}}} \quad (4)$$

where γ_{\min} denotes the minimum strength factor. The strength and flutter constraints are as follows:

$$\sigma_{\text{compressive}} < F_{\text{compressive}} \quad (5a)$$

$$\sigma_{\text{tension}} < F_{\text{tension}} \quad (5b)$$

$$\sigma_{\text{shear}} < F_{\text{shear}} \quad (5c)$$

$$V_F > V_{F_{\text{required}}} \quad (5d)$$

$$t_i > t_{\min} \quad (5e)$$

Figure 3 shows the convergence history of structural optimization for the initial geometry.

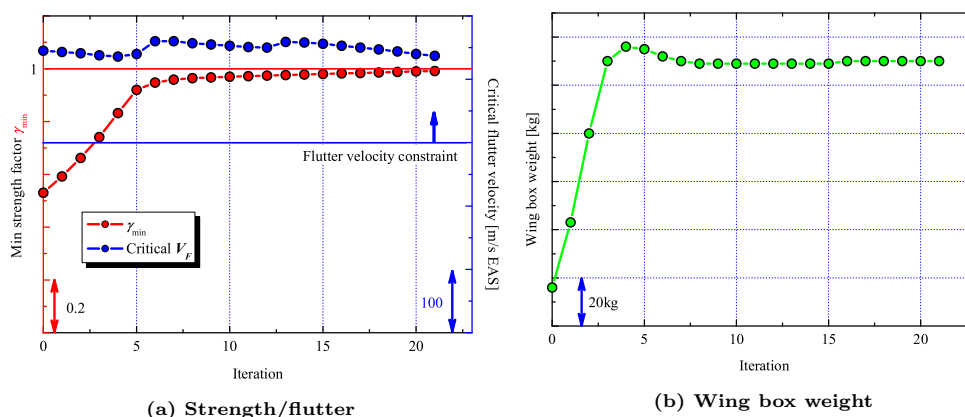


Figure 3. Convergence histories of each characteristic for the initial geometry.

2. Static Aeroelastic Analysis

First, in this module, Euler computation is carried out on an aerodynamic unstructured mesh. As surface pressure data can be obtained, surface force is computed using the FLEXCFD MHI in-house code as an interface between aerodynamics and structures. Then, the displacement is calculated from the surface force using NASTRAN. When this displacement is converged, the static aeroelastic analysis module is finished. When it is not converged, the aerodynamic mesh is moved using the unstructured dynamic mesh method^{5,6} to re-calculate Euler computation. As it was assumed that the planform was fixed in the present study, only displacement in the z -direction was employed in the unstructured dynamic mesh method. The decision of displacement convergence was employed using the following equations:

$$\begin{cases} \left| \frac{C_L(n) - C_L(n-1)}{C_L(n-1)} \right| \leq 0.0001 & \text{if } |C_L| \text{ is small} \\ \left| \frac{C_L(n) - C_L(n-1)}{C_L(n-1)} \right| \leq 0.001 & \text{otherwise} \end{cases} \quad (6)$$

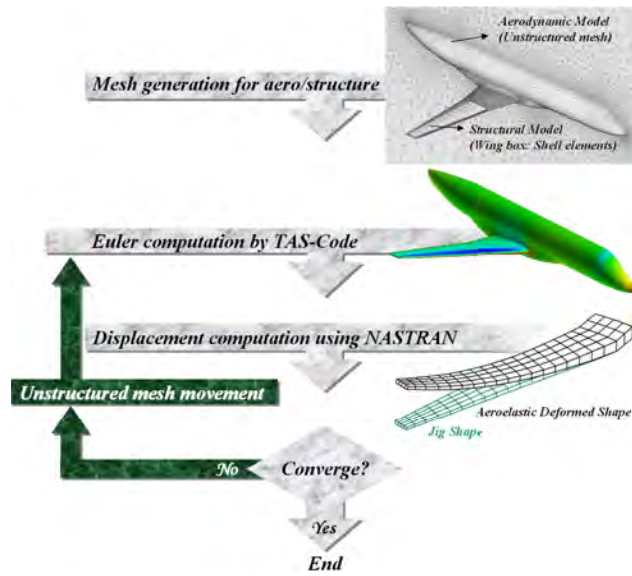
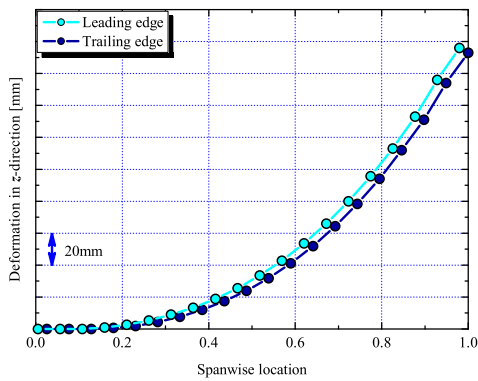
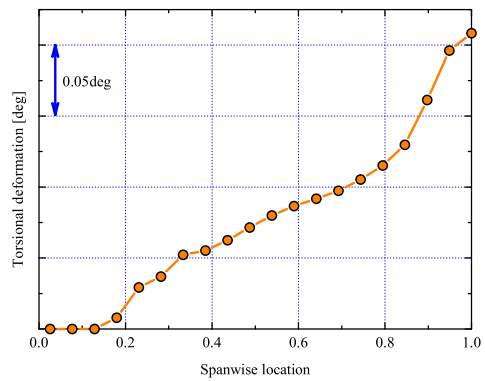


Figure 4. Flowchart of static aeroelastic analysis. The displacement is enlarged by a factor 10 to emphasize aeroelastic deformed shape.



(a) Deformation in z -direction at leading/trailing edge



(b) Torsional deformation (positive: pitch-up)

Figure 5. Static aeroelastic deformation of the initial geometry.

The flowchart of this module is shown in Fig. 4, and the results of static aeroelastic analysis for the initial geometry are shown in Fig. 5. The displacement computed by the present static aeroelastic analysis usually converges after three iterations.

3. Aerodynamic Evaluation

In the present study, TAS-Code was employed for aerodynamic evaluation. The three-dimensional Reynolds-averaged Navier-Stokes (RANS) equations were computed with a finite-volume cell-vertex scheme. The unstructured hybrid mesh method¹⁷ was applied to capture the boundary layer accurately and efficiently. The Harten-Lax-van Leer-Einfeldt-Wada Riemann solver¹⁸ was used for the numerical flux computations. The Venkatakrishnan's limiter¹⁹ was applied when reconstructing the second order accuracy. The lower-upper symmetric-Gauss-Seidel implicit scheme²⁰ was applied for time integration. Figure 6 shows the unstructured CFD mesh and the wing box element for the structural FEM model. Moreover, Fig. 7 shows the unstructured meshes for Euler and N-S computations. For the N-S computations, prism layers were stacked in 20 layers on the body surface.

With regard to the turbulence model, the Spalart-Allmaras one-equation model modified by Dacles-Mariani *et al.*²¹ was employed without transition. This model was confirmed to be effective for capturing the complex vortex structure²².

Euler and RANS computations were carried out under subsonic and transonic flight conditions, respectively. Taking advantage of the parallel search in EAs, the present optimization was parallelized on vector-parallel machines (NEC SX-5 and SX-7). The master processing element (PE) managed ARMOGA, while the slave PEs computed aerostructural evaluation processes. Slave processes did not require synchronization.

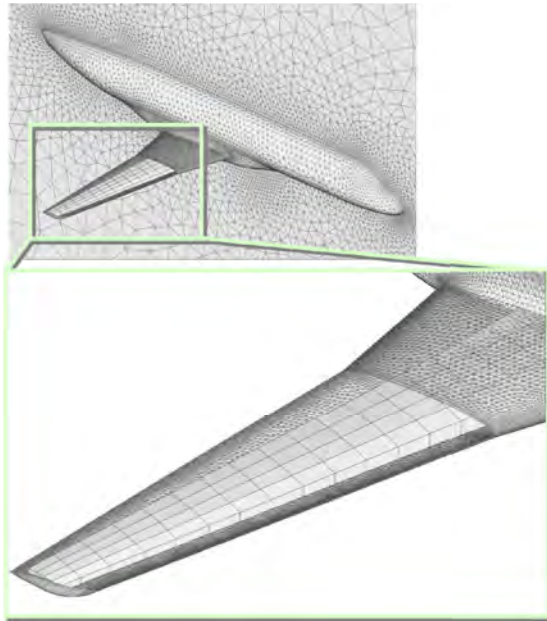


Figure 6. Visualization between unstructured surface mesh for aerodynamic CFD model and wing box element for structural FEM model.

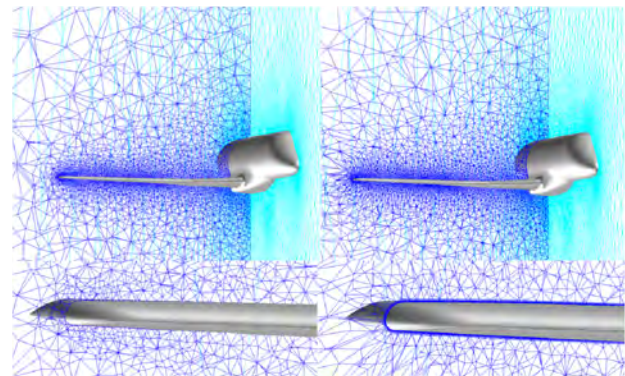


Figure 7. Visualization of unstructured volume meshes; Left is generated by all tetrahedron mesh for Euler computation. Right is generated by hybrid mesh for N-S computation. Lower are close-up views in the vicinity of respective wing tip.

4. Flight Envelope Analysis

Finally, the Block Fuel Module was executed to evaluate three objective functions as block fuel, maximum takeoff weight, and drag divergence, and to check the constraints for flight conditions shown in Fig. 2. In this module, the wing box weight for structural-optimized shape and aerodynamic performance were used as input. As all eight individuals were evaluated, the work of the slave PEs was finished in one generation.

III. Optimization Results

The population size was set to eight, and then roughly 70 Euler and 90 RANS computations were performed in one generation. It took roughly one and nine hours of CPU time on NEC SX-5 and SX-7 per PE for single Euler and RANS computations, respectively. The population was re-initialized every five generations for the range adaptation. First, evolutionary computation was performed for 17 generations. Then, the evolutionary operation was restarted using eight non-dominated solutions extracted from all solution of 17 generations, and two more generations were computed. A total evolutionary computation of 19 generations was carried out. The evolution may not converge yet. However, the results were satisfactory because several non-dominated solutions achieved significant improvements over the initial design. Furthermore, a sufficient number of solutions were searched such that the sensitivity of the design space around the initial design could be analyzed. This will provide useful information for designers.

All solutions evaluated are shown in Fig. 8, and Fig. 9 shows all solutions projected on a two-dimensional plane between two objectives, the block fuel, and the drag divergence. As this figure shows that the non-dominated front was generated, there was a tradeoff between the block fuel and the drag divergence. All solutions projected on two-dimensional planes between other combinations were shown in Figs. 10 and 11. As the non-dominated solutions did not comprise Pareto front, these figures showed that there were no global tradeoff between these combinations of the objective functions.

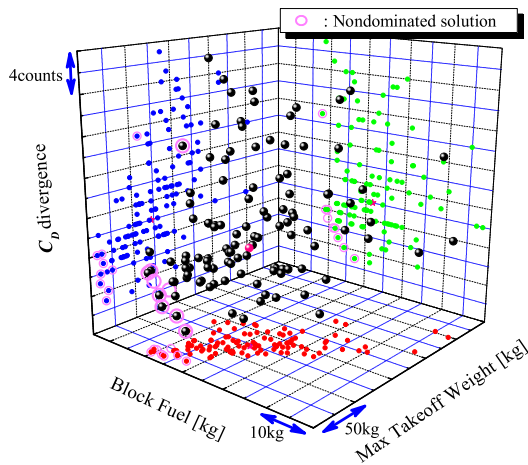


Figure 8. All solutions plotted in three-dimensional space of all objective functions.

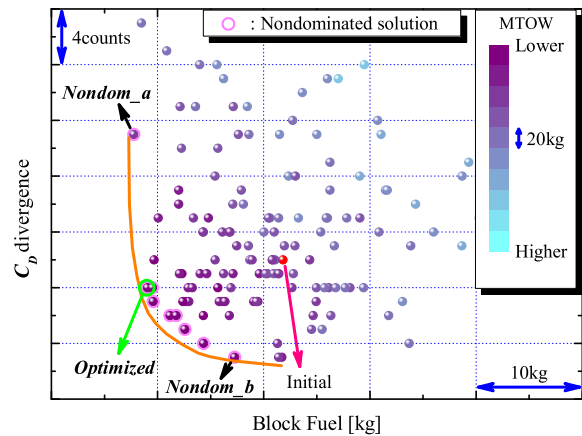


Figure 9. All solutions on two-dimensional plane between block fuel and C_D divergence.

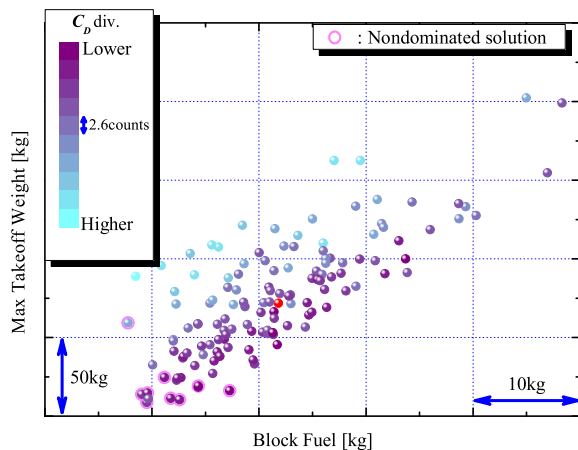


Figure 10. All solutions on two-dimensional plane between block fuel and maximum takeoff weight.

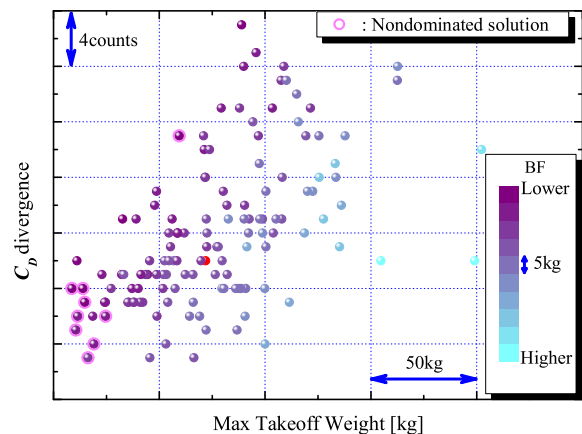


Figure 11. All solutions on two-dimensional plane between maximum takeoff weight and C_D divergence.

A. Comparison between Initial and Optimized Geometries

Although the wing box weight tends to increase as compared with that of the initial geometry, the block fuel can be reduced. Thus, the aerodynamic performance can redeem the penalty due to the structural weight. An individual on the non-dominated front shown in Fig. 9 was selected, indicated as ‘*optimized*’, and then the *optimized* geometry was compared with the initial geometry.

Figure 12 shows each displacement obtained by static aeroelastic analysis. This figure shows that the displacements were not markedly different between upward and downward on the leading and trailing edges. Whereas, twisting displacement was slightly reduced in the vicinity of the kink as 35.0% spanwise location, and then the outboard wing was bent upward as a whole. These phenomena predict reduction of the shock wave near the kink, *i.e.*, reduction of wave drag, and an increase in the generation of C_L at the outboard wing.

Figures 13 and 14 show a comparison of polar curves. Although the drag minimization was not considered here, C_D was reduced. The sensitivity of aerodynamic performance, such as C_L , C_D , and C_{Mp} , to angle of attack α did not depend on Mach numbers very much. By comparison of the polar curves at constant C_L for the cruising condition, C_D of the *optimized* geometry was found to be reduced by 5.5 counts. Due to the improvement of the drag, the block fuel of the *optimized* geometry was decreased by over one percent even with its structural weight penalty.

Next, the mechanism of the drag reduction was investigated. Figure 15 shows a comparison of the spanwise distributions of C_L and C_D of the initial and *optimized* geometries. This figure shows that the drag decreased at the 35.0% spanwise location. Figure 16 shows a comparison of the pressure distributions at the 35.0% spanwise location. Then, the variation in the leading-edge bluntness works to depress the shock wave on the upper wing surface, *i.e.*, to reduce the wave drag. In fact, the pressure drag coefficient was reduced by 5.6 counts. Figure 17 shows a comparison of the shock wave visualized by the shock function F_{shock}^{23} , which is given as follows:

$$F_{\text{shock}} = \frac{\mathbf{V} \cdot \nabla P}{a \cdot |\nabla P|} \quad (7)$$

where \mathbf{V} is the velocity vector, P is pressure, and a denotes the local speed of sound.

The shock wave of the optimized geometry was weaker than that of the initial geometry in the vicinity of the 35.0% spanwise location as shown in Fig. 17 indicating the wave drag reduction. Moreover, the vorticity of the wing wake of the *optimized* geometry in the vicinity of the 35.0% spanwise location was weaker than that of the initial geometry as shown by helicity contours in Fig. 18. Therefore, these figures show that the shape change near the 35.0% spanwise location, *i.e.*, the shape modification in the vicinity of the kink is effective to reduce the drag. Figure 18 also shows strong vortices in the vicinity of the fairing. Thus, improvement of fairing design should be considered in future.

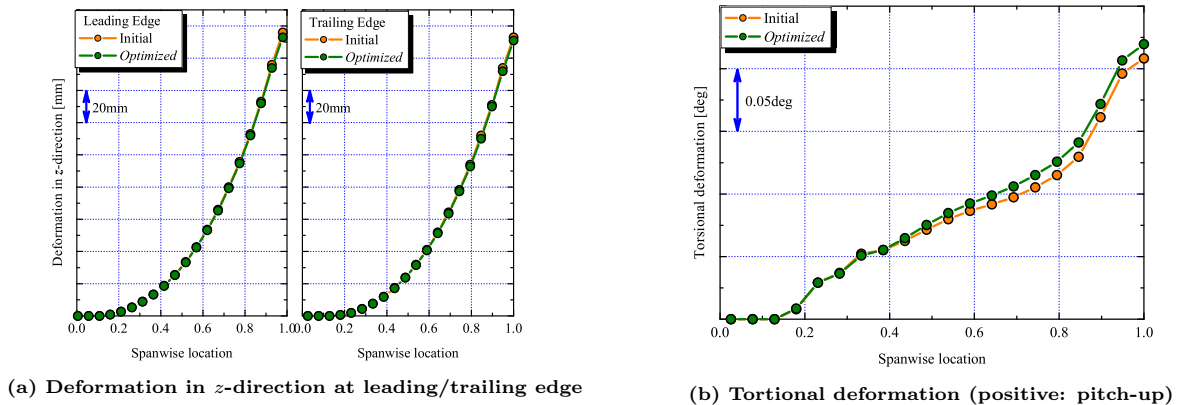


Figure 12. Comparison of static aeroelastic deformation between initial and *optimized* geometries.

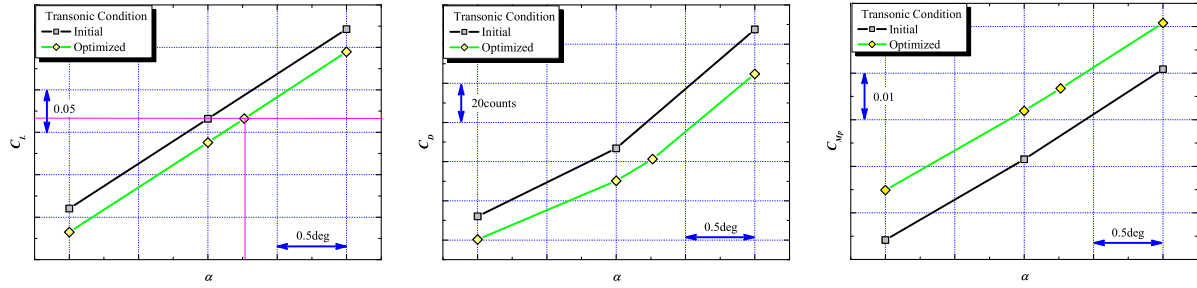


Figure 13. Comparison of the polar curves of C_L - α , C_D - α and C_{M_p} - α between initial and *optimized* geometries under transonic flight condition.

B. Comparison between Weak Non-dominated Solutions with Regard to Block Fuel

Figures 9 to 11 show that there is a tradeoff only between block fuel and C_D divergence. To investigate the geometric sensitivity to the primary objective, block fuel, aerodynamic performance was compared between weak non-dominated solutions. Left-side and right-side weak non-dominated solutions are named as ‘*Nondom_a*’ and ‘*Nondom_b*’, respectively in Fig. 9.

Figure 19 shows displacements obtained by static aeroelastic analysis. This figure shows no marked differences in upward or downward displacements on both the leading and trailing edges. However, there was a difference in twisting between the 50% to 85% spanwise location. Figures 20 and 21 show the polar curves under subsonic and transonic flight conditions. C_L - C_D curves of both flight conditions appear very similar. It should be noted that C_D is more sensitive to α . Although there were no differences in the sensitivity of C_L and C_{M_p} to α , the increase ratios of C_D were different as shown in C_D - α curves in Fig. 20. This tendency was pronounced more when the Mach number increased. This result indicated that the C_D increase follows the C_L increase to achieve an increase in L/D . In fact, *Nondom_a* geometry showed an L/D increase of roughly 3.2% at the cruise condition as compared with *Nondom_b*. Therefore, under subsonic and transonic flight conditions L/D is found highly related to block fuel improvements. Especially, transonic L/D was more sensitive because of its nonlinearity in α .

The mechanism of L/D increase depends on the bluntness of the upper surface of the leading edge. The PARSEC design variable $r_{LE_{lo}}/r_{LE_{up}}$, which is the leading-edge bluntness ratio between the lower and upper surfaces, for *Nondom_a* was one-tenth higher than the value for *Nondom_b* at the 35.0% spanwise location. Therefore, the curvature of *Nondom_b* was smaller, shock wave becomes weaker, and then wave drag reduced. Figure 22 shows C_p distributions at three spanwise locations. The shock wave on the wing of *Nondom_b* as a whole was clearly depressed. This result was also confirmed on the shock wave visualization shown in Fig. 23. However, helicity contours did not show a clear distinction in Fig. 24. Thus, the C_D decrease may be dependent only on the wave drag.

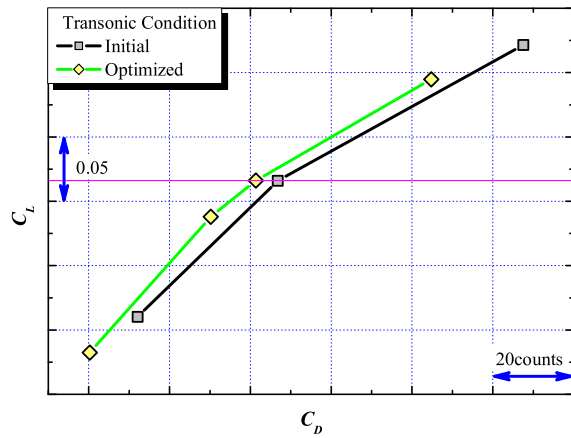


Figure 14. Comparison of the C_L - C_D curves between initial and *optimized* geometries under transonic flight condition.

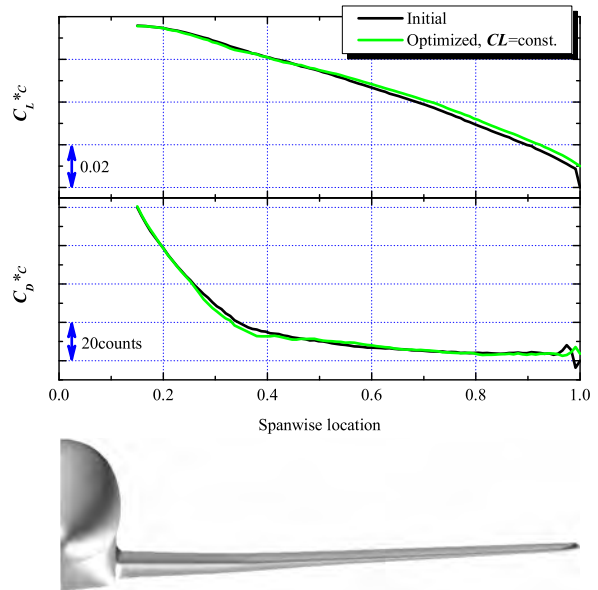


Figure 15. Comparison of C_L and C_D spanwise distributions between initial and *optimized* geometries under transonic cruising flight condition. C_L is constant.

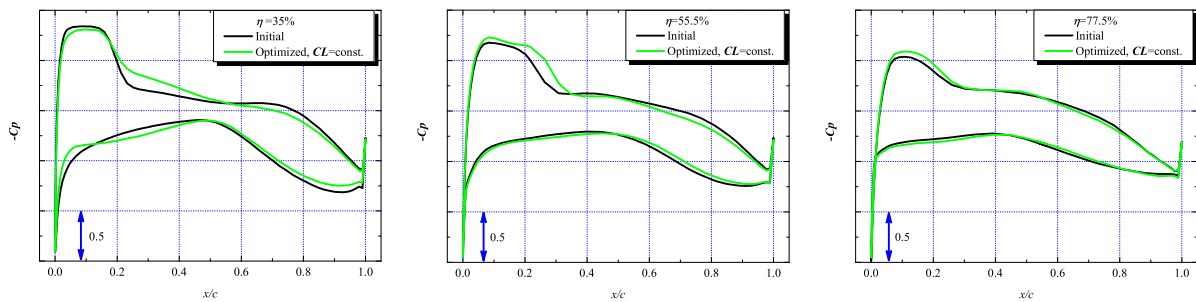


Figure 16. Comparison of C_p distributions between initial and *optimized* geometries under transonic cruising flight condition at 35.0, 55.5, and 77.5% semispan locations, respectively. C_L is constant.



Figure 17. Comparison of shock wave visualizations colored by entropy under the transonic cruising flight condition between initial (left) and *optimized* (right) geometries. C_L is constant.

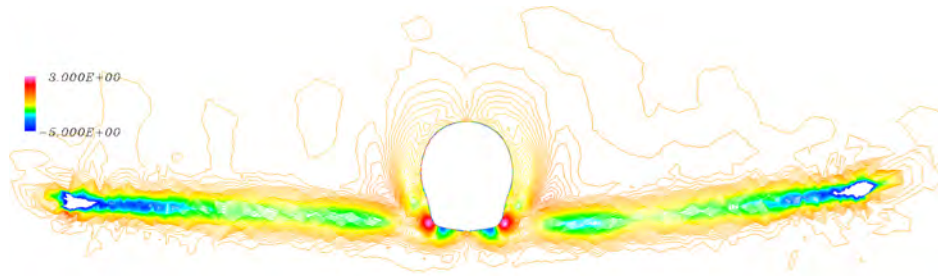


Figure 18. Comparison of helicity contours of wing wake of $x/L = 0.7$ under the transonic cruising flight condition between initial (left) and *optimized* (right) geometries. C_L is constant. Vortical rotation direction is colored symmetrically.

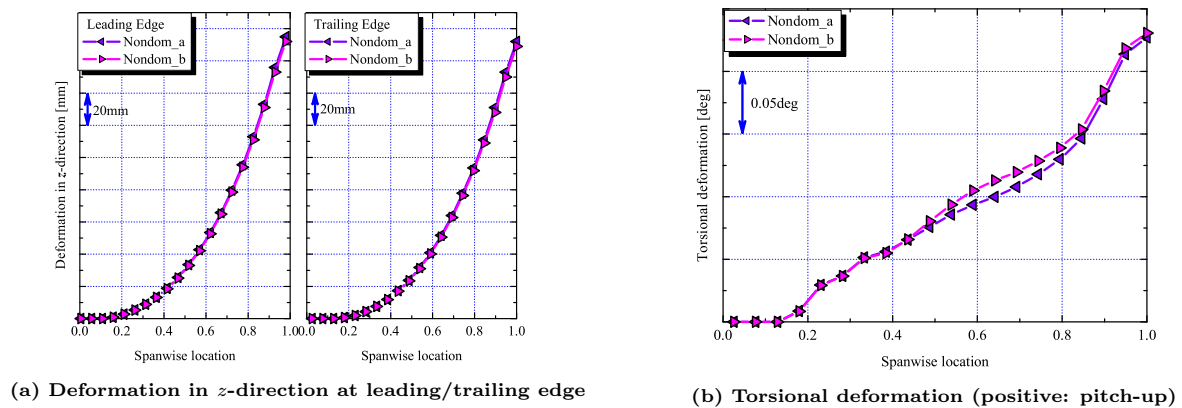


Figure 19. Comparison of static aeroelastic deformation between weak non-dominated solutions.

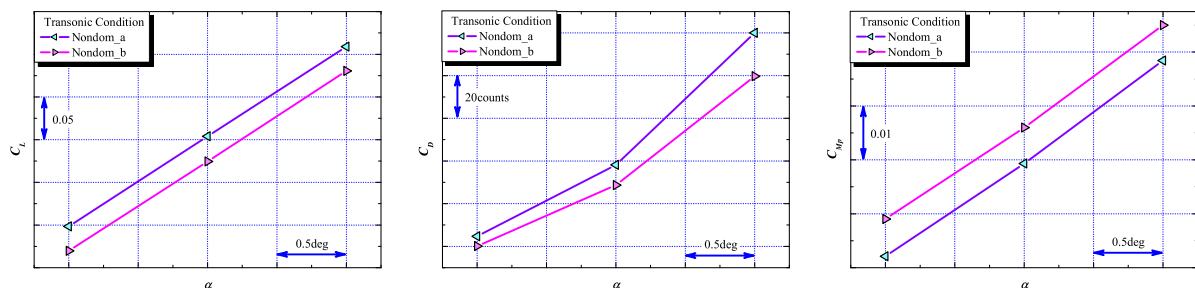


Figure 20. Comparison of the polar curves of C_L - α , C_D - α and C_{M_p} - α between weak non-dominated solutions geometries under transonic cruising flight condition.

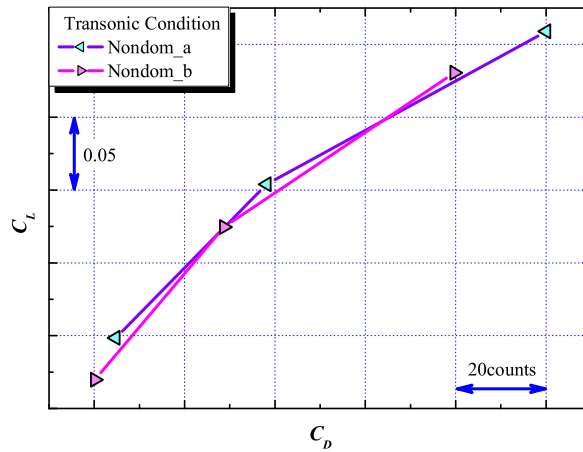


Figure 21. Comparison of the C_L - C_D curves between weak non-dominated solutions under transonic cruising flight condition.

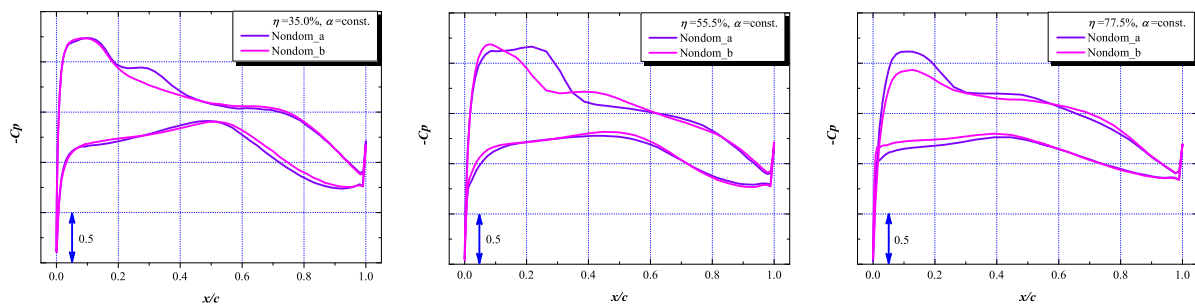


Figure 22. Comparison of the pressure distributions between weak non-dominated solution geometries under transonic cruising flight condition at 35.0, 55.5 and 77.5% semispan locations, respectively.



Figure 23. Comparison of shock wave visualizations colored by entropy under the transonic cruising flight condition between weak non-dominated solutions of *nondom_a* (left) and *nondom_b* (right) geometries.

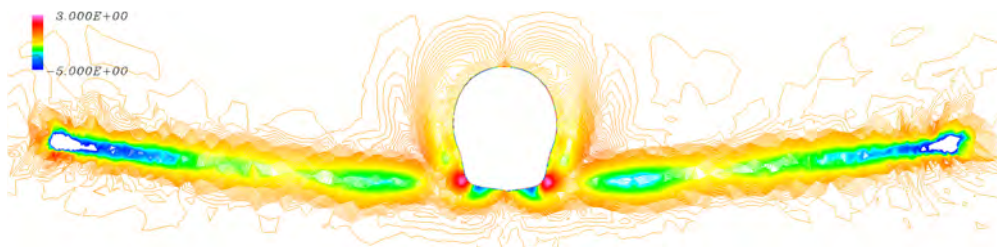


Figure 24. Comparison of helicity contours of wing wake of $x/L = 0.7$ under the transonic cruising flight condition between weak non-dominated solutions of *nondom_a* (left) and *nondom_b* (right) geometries. Vortical rotation direction is colored symmetrically.

IV. Data Mining

If the optimization problem has only two objectives, tradeoffs can be visualized easily. However, if there are more than two objectives, the technique to visualize the computed non-dominated solutions is needed. Therefore, in the present study, Self-Organizing Maps (SOMs) proposed by Kohonen²⁴ were employed.

A. Self-Organizing Map

SOM is a technique not only for visualization but also a tool for the intelligent compression of information. That is, SOM can be applied for data mining to acquire knowledge regarding the design space. In the present study, Viscovery[®] SOMine²⁵ (Eudaptics GmbH, Austria) was employed.

1. Neural Network and SOMs

SOM is a two-dimensional array of neurons:

$$M = \{\mathbf{m}_1 \cdots \mathbf{m}_{p \times q}\} \quad (8)$$

One neuron is a vector called the codebook vector:

$$\mathbf{m} = [m_{i_1} \cdots m_{i_n}] \quad (9)$$

This has the same dimension as the input vectors. The neurons are connected to adjacent neurons by a neighborhood relation. This dictates the topology, or the structure, of the map. Usually, the neurons are connected to each other via rectangular or hexagonal topology. One can also define a distance between the map units according to their topology relations. Immediate neighbors (the neurons that are adjacent) belong to the neighborhood N_c of the neuron \mathbf{m}_c . The neighborhood function should be a decreasing function of time:

$$N_c = N_c(t) \quad (10)$$

The training consists of drawing sample vectors from the input data set and “teaching” them to the SOM. The teaching consists of choosing a winner unit by the means of a similarity measure and updating the values of codebook vectors in the neighborhood of the winner unit. This process is repeated a number of times. In one training step, one sample vector is drawn randomly from the input data set. This vector is fed to all units in the network and a similarity measure is calculated between the input data sample and all the codebook vectors. The best-matching unit is chosen to be the codebook vector with greatest similarity with the input sample. The similarity is usually defined by means of a distance measure. For example in the case of Euclidean distance the best-matching unit is the closest neuron to the sample in the input space.

The best-matching unit, usually noted as \mathbf{m}_c , is the codebook vector that matches a given input vector \mathbf{x} best. It is defined formally as the neuron for which

$$\|\mathbf{x} - \mathbf{m}_c\| = \min_i [\|\mathbf{x} - \mathbf{m}_i\|] \quad (11)$$

After finding the best-matching unit, units in the SOM are updated. During the update procedure, the best-matching unit is updated to be a little closer to the sample vector in the input space. The topological neighbors of the best-matching unit are also similarly updated. This update procedure stretches the best-matching unit and its topological neighbors towards the sample vector. The codebook vectors are situated in the crossings of the solid lines. The topological relationships of the SOM are drawn with lines. The input fed to the network is marked by \mathbf{x} in the input space. The best-matching unit, or the winner neuron is the codebook vector closest to the sample, in this example the codebook vector in the middle above \mathbf{x} . The winner neuron and its topological neighbors are updated by moving them a little towards the input sample. The neighborhood in this case consists of the eight neighboring units in the figure. The updated network is shown in the same figure with dashed lines.

2. *Viscovery SOMine*

Although SOMine is based on the SOM concept and algorithm, it employs an advanced variant of unsupervised neural networks, *i.e.* Kohonen's Batch-SOM.

The algorithm consists of two steps that are iteratively repeated until no more significant changes occur. First the distances between all data items $\{\mathbf{x}_i\}$ and the model vectors $\{\mathbf{m}_j\}$ are computed and each data item \mathbf{x}_i is assigned to the unit c_i that represents it best.

In the second step, each model vector is adapted to better fit the data it represents. To ensure that each unit j represents similar data items as its neighbors, the model vector \mathbf{m}_j is adapted not only according to the assigned data items but also in regard to those assigned to the units in the neighborhood. The neighborhood relationship between two units j and k is usually defined by a Gaussian-like function

$$h_{jk} = \exp\left(-\frac{d_{jk}^2}{r_t^2}\right) \quad (12)$$

where d_{jk} denotes the distance between the units j and k on the map, and r_t denotes the neighborhood radius which is set to decrease with each iteration t .

Assuming a Euclidean vector space, the two steps of the Batch-SOM algorithm can be formulated as

$$c_i = \arg \min \|\mathbf{x}_i - \mathbf{m}_j\| \quad (13a)$$

$$\mathbf{m}_j^* = \frac{\sum_i h_{jc_i} \mathbf{x}_i}{\sum_i h_{jc_i}} \quad (13b)$$

where \mathbf{m}_j^* is the updated model vector.

In contrast to the standard Kohonen algorithm, which makes a learning update of the neuron weights after each record being read and matched, the Batch-SOM takes a 'batch' of data, typically all records, and performs a 'collected' update of the neuron weights after all records have been matched. This is much like 'epoch' learning in supervised neural networks. The Batch-SOM is a more robust approach, since it mediates over a large number of learning steps. Most important, no learning rate is required. The SOMine implementation combines four enhancements to the plain Batch-SOM algorithm (See Ref.²⁶ for more details). In SOMine, the uniqueness of the map is ensured by the adoption of the Batch-SOM and the linear initialization for input data.

Much like some other SOMs²⁷, SOMine creates a map in a two-dimensional hexagonal grid. Starting from numerical, multivariate data, the nodes on the grid gradually adapt to the intrinsic shape of the data distribution. Since the order on the grid reflects the neighborhood within the data, features of the data distribution can be read off from the emerging map on the grid.

In SOMine, the trained SOM is systematically converted into visual information. The tool provides an extensive built-in capability for both pre-processing and post-processing as well as for the automatic color-coding of the map and its components. SOMine is particularly useful in the determination of dependencies between variables as well as in the analysis of high-dimensional cluster distributions.

3. *Cluster Analysis*

Once SOM projects input space on a low-dimensional regular grid, the map can be utilized to visualize and explore properties of the data. When the number of SOM units is large, to facilitate quantitative analysis of the map and the data, similar units need to be grouped, *i.e.*, clustered. The two-stage procedure — first using SOM to produce the prototypes which are then clustered in the second stage — was reported to perform well when compared to direct clustering of the data²⁷.

Hierarchical agglomerative algorithm is used for clustering here. The algorithm starts with a clustering where each node by itself forms a cluster. In each step of the algorithm two clusters are merged: those with minimal distance according to a special distance measure, the SOM-Ward distance²⁵. This measure takes into account whether two clusters are adjacent in the map. This means that the process of merging clusters is restricted to topologically neighbored clusters. The number of clusters will be different according to the hierarchical sequence of clustering. A relatively small number will be chosen for visualization, while a large number will be used for generation of codebook vectors for respective design variables.

B. Knowledge in the Design Space

1. Tradeoff Analysis of the Design Space

All of the solutions have been projected onto the two-dimensional map of SOM. Figure 25 shows the resulting SOM with 11 clusters considering the three objectives. Furthermore, Fig. 26 shows the SOMs colored by the three objectives. These color figures show that the SOM indicated in Fig. 25 can be grouped as follows: The upper left corner corresponds to the designs with high block fuel and maximum takeoff weight. The left center area corresponds to designs with high maximum takeoff weight and C_D divergence. The lower left corner corresponds to designs with low block fuel and high C_D divergence. Figure 26(a) and Fig. 26(c) show that there is a tradeoff between these two objective functions. The lower center area corresponds to designs with low block fuel. The right hand side corresponds to designs with low C_D divergence. As the coloring in Fig. 26(a) is similar to that in Fig. 26(b), there was not a severe tradeoff between the block fuel and the maximum takeoff weight. The lower right corner corresponds to designs with low value of all objectives. Extreme non-dominated solutions are indicated in Fig. 26(a) to (c). As they are in different clusters, the simultaneous optimization of the three objectives is impossible. However, the lower right cluster has relatively low values for all three objectives. Thus, this region of the design space may provide a sweet spot for the present design problem.



Figure 25. SOM of all solutions in the three-dimensional objective function space.

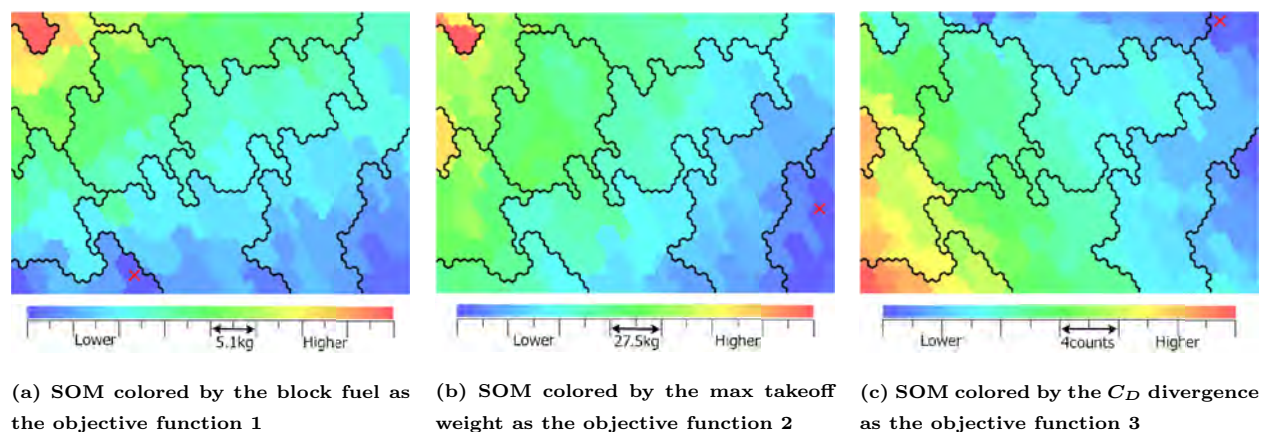


Figure 26. SOM colored by the objective functions. The symbol \times denotes the respective extreme non-dominated solutions.

2. Effects of Aerodynamic Performance on Objective Functions

Figure 27 shows the SOMs colored by the aerodynamic performance under transonic cruising flight condition. Figures 27(a) and (b) show the SOMs colored by C_L and C_D , respectively. As these figures show similar coloring, the L/D increase is not so easy. Lower C_D values are located in the lower right corner in Fig. 27(b). As this area clusters designs with low value of all objectives, this observation suggests that when all objectives are optimized simultaneously, the C_D under the cruising flight condition is also reduced. Furthermore, as the clusters of lower values of the maximum takeoff weight shown in Fig. 26(b) appears on the right hand side of the map, C_D can be decreased simultaneously with the maximum takeoff weight. As the area with higher C_D shown in Fig. 27(b) generally coincide with the area with higher objective function values, C_D is a very important performance index.

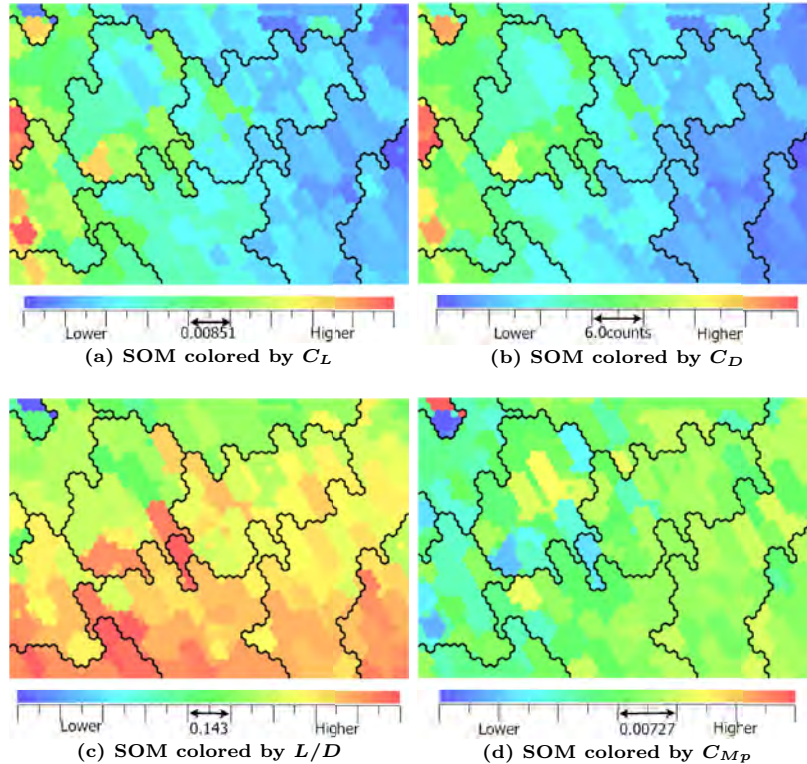


Figure 27. SOM colored by aerodynamic performance under transonic cruising flight condition.

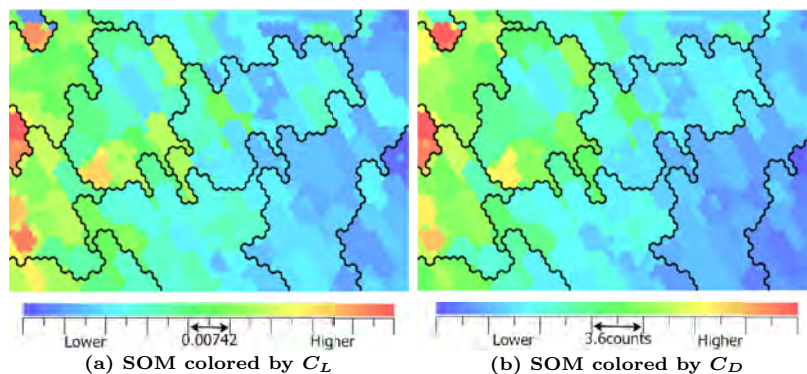


Figure 28. SOM colored by aerodynamic performance under subsonic flight condition.

Figure 27(c) shows the SOM colored by L/D ; lower values are located in the upper left corner. As the higher values of the block fuel shown in Fig. 26(a) are present at the same location, lower L/D makes the

block fuel worse. Furthermore, higher L/D values are located in the lower area shown in Fig. 27(c). As the lower values of the block fuel shown in Fig. 26(a) are present at the same area, higher L/D was effective to decrease the block fuel. However, higher transonic L/D values were not necessarily effective to reduce the block fuel in Fig. 27(c) because not only the cruise condition but also the complete flight profile from takeoff to landing were considered in the present study.

Figure 27(d) shows the SOM colored by C_{Mp} . When C_{Mp} increases and C_L decreases and L/D is reduced. C_L and C_D increase with decreasing C_{Mp} . That is, a decrease in C_{Mp} makes the objective function values worse.

Figure 28 shows the SOM colored by C_L and C_D under subsonic flight condition. As the resulting SOMs appear similar to transonic C_L and C_D shown in Fig. 27(a) and (b), their influences to the objective functions were also the same. That is, the effects of subsonic aerodynamic performance on objective functions might be predicted from the effects of transonic aerodynamic performance in the present study.

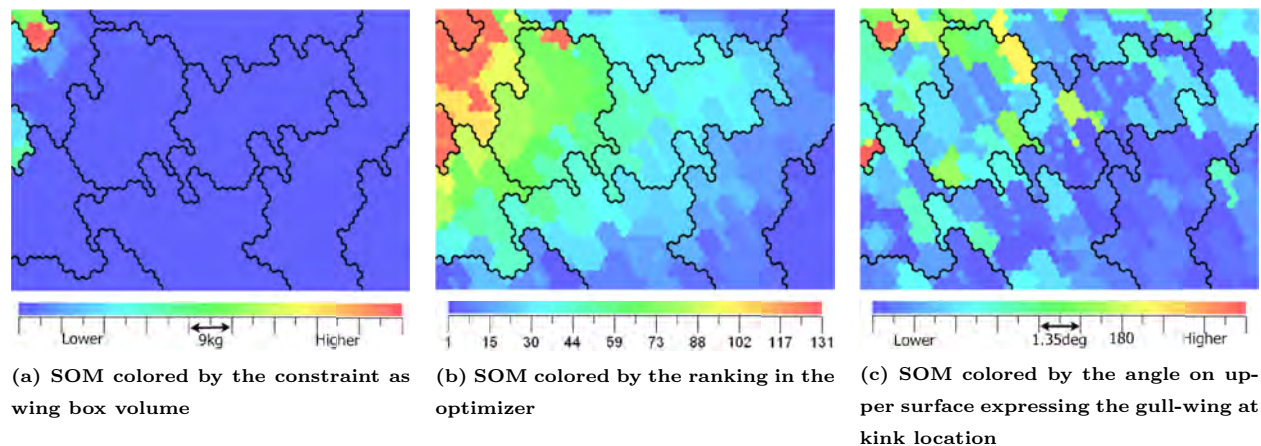


Figure 29. SOM colored by the characteristic values.

3. Additional Characteristics

Figure 29 shows the SOM colored by three other characteristic values. Figure 29(a) shows the SOM colored by the constraints of the evaluated fuel mass. The colored values are defined as follows:

$$Value = Volume_{\text{required fuel}} - Volume_{\text{fuel capacity}} \quad (14)$$

where, $Volume_{\text{required fuel}}$ denotes the fuel volume required to fly the given range, and $Volume_{\text{fuel capacity}}$ denotes the fuel capacity volume that can actually be carried in the wing. When this value is greater than zero, the aircraft cannot fly the given range. As the area with values of over zero corresponds to the area with high maximum takeoff weight, the aerodynamic characteristics and design values that have effects on maximum takeoff weight dominate this constraint.

Figure 29(b) shows the SOM colored by the ranking in the optimizer. As the upper left region has a poorer ranking, larger block fuel and maximum takeoff weight as objective functions 1 and 2 dominate the poor ranking. In contrast, the lower left area with higher C_D divergence does not have poor ranking. These observations indicate that improvement in C_D divergence is not dominated by the specific aerodynamic performance and design variables, and further improvement cannot be achieved by the present problem easily.

Figure 29(c) shows the SOM colored by the angle between inboard and outboard on the upper wing surface for the gull-wing at the kink location. Angles greater and less than 180 deg correspond to gull and inverted gull-wing, respectively. The characteristic inverted gull-wing shape is shown in Fig. 30. The locations of higher values of this angle as shown in Fig. 29(c) correspond to positions of higher C_D under the transonic cruising flight condition shown in Fig. 27(b). However, at angles less than 180 deg, there was little correlation between Fig. 27(b) and Fig. 29(c). The inverted gull-wing did not affect aerodynamic performance. The inverted gull-wing is known to have a structural weight increase, which is also observed in



Figure 30. Visualization of a characteristic inverted gull-wing.

the present results. Indeed, the locations of higher angles in Fig. 29(c) had higher maximum takeoff weights as shown in Fig. 26(b). Therefore, non-gull wings should be designed in future.

4. Effects of Design Variables

Finally, Fig. 31 and Fig. 32 show the SOMs colored by the selected design variables with regard to the PARSEC airfoil parameters at 35.0% and 55.5% spanwise locations, respectively. Moreover, Fig. 33 shows the SOM colored by the design variable, twist angle. The design variables can be summarized as follows, taking into consideration the effects on each objective function and aerodynamic performance.

There are no design variables that show large effects on objective function 1 as block fuel. The large twist angles at the 35.0% spanwise location makes objective function 2 as maximum takeoff weight worse. In addition, large twist angles at the 55.5% spanwise location increase objective function 3 as C_D divergence. However, no design variable of the PARSEC airfoil had apparent effects on any objective functions by itself. As shown later, PARSEC design variables have direct effects on aerodynamic performances. However, the present objective functions are not pure aerodynamic characteristics. Therefore, effects of the design variables on the objective functions were not trivial. There were no design variables and no aerodynamic characteristics that were effective on the sweet spot with relatively low values for all three objective functions. Therefore, the individual that resides in the sweet spot cannot be generated by hand. A correlation between objective function and design variable is desirable when the sensitivity of the design variable is to be investigated; this is one of the important aspects in optimization problems in general.

Next, the effects of design variables on aerodynamic performance were investigated. From the correspondence between Figs. 27, 31, 32, and 33, the effects of respective design variables are summarized in Tables 2 to 4. These tables indicate that the design variables of the PARSEC airfoil have effects on aerodynamic performance directly. It is noted that the effects of design variables to C_D can be predicted from the above results because Figs. 27(a) and (b) are similar. Furthermore, the effects of design variable on aerodynamic performance under the subsonic flight condition can be predicted because the SOMs appeared similar at the transonic and subsonic flight conditions as shown in Figs. 27 and 28. The leading-edge curvature of PARSEC airfoil at 35.0% spanwise location was effective to L/D and C_{Mp} .

The geometry near the 55.5% spanwise location was not changed markedly with regard to twist angle, as shown in Fig. 33(b). The geometry near the 96.0% spanwise location was changed to upward twisting. Conversely, the geometry near the 35.0% spanwise location was changed to downward twisting. The improvement in the vicinity of the 35.0% spanwise location restrained the shock wave, reducing the wave drag shown in Fig. 17. When the drag decreases, the lift may decrease simultaneously. The lift was increased to compensate for the reduction in the vicinity of the kink so that the angle of attack of the outboard wing was increased although the wing is still twisted down. It should be noted that the angle of attack near the kink had an effect on the transonic drag, especially as shown in Fig. 33(a). This corresponds to the phenomena shown in Fig. 17. Specifically, the shock wave in the vicinity of the kink is weakened. The angle of attack near the kink with downward twisting is replaced from the initial geometry and the lost lift is made up to replace the angle of attack at the outboard wing with upward twisting so that the wave drag is reduced near the kink. Upward twisting at the outboard wing has no influence on transonic drag, as shown in Fig. 33(c). This corresponds to the prediction shown in Fig. 12. The other design variables were not effective to reduce the objective functions or to increase aerodynamic performance as C_D and L/D under transonic cruise flight condition. Data Mining techniques using SOM were found to be able to classify the design variables considering their influence on the objectives and aerodynamic performance.

Design knowledge regarding the block fuel, which is the most important element of the present optimiza-

Table 2. Effects of design variables to C_L under transonic cruising flight condition.

<i>design variable</i>		C_L
PARSEC α_{TE} @ 35.0%	decrease	increase
PARSEC x_{up} @ 55.5%	increase	increase
PARSEC x_{lo} @ 55.5%	decrease	increase
Twist @ 35.0%	increase	increase
Twist @ 55.5%	increase	increase

Table 3. Effects of design variables to L/D under transonic cruising flight condition.

<i>design variable</i>		L/D
PARSEC $r_{LE_{lo}}/r_{LE_{up}}$ @ 35.0%	decrease	decrease
PARSEC $z_{xx_{lo}}$ @ 55.5%	increase	decrease

Table 4. Effects of design variables to C_{Mp} under transonic cruising flight condition.

<i>design variable</i>		C_{Mp}
PARSEC α_{TE} @ 35.0%	decrease	decrease
PARSEC β_{TE} @ 35.0%	decrease	decrease
PARSEC $r_{LE_{lo}}/r_{LE_{up}}$ @ 35.0%	decrease	increase
PARSEC x_{up} @ 55.5%	increase	decrease
PARSEC x_{lo} @ 55.5%	decrease	decrease
PARSEC $z_{xx_{lo}}$ @ 55.5%	increase	increase

tion problem, will be considered. The following two points are the keys to improve the block fuel: 1) L/D increase, 2) $dC_D/d\alpha$ increase, at any Mach number. However, there were no single design variable in the present design space capable of satisfying them simultaneously. In fact, this was confirmed by the SOMs. Although PARSEC design variables correspond to aerodynamic performances, there are no direct effects on other objective functions. It would be easier to understand the design space if the design variables have direct influences to the objective functions.

C. Evaluation of the Non-Gull Geometry

The design knowledge obtained by SOM shows that a non-gull wing should be designed. Therefore, we modified the optimized wing shape which achieved the highest improvement in the block fuel to the non-gull wing shape (called as '*optimized_mod*') to verify the design knowledge obtained by the previous Data Mining.

The result is shown in Figs. 34 to 36. These figures show that *optimized_mod* improves both block fuel and maximum takeoff weight. Moreover, by comparison of the polar curves at constant C_L for cruising condition shown in Fig. 37, C_D of *optimized_mod* was found to be reduced by 10.6 counts over the initial geometry. Due to the improvement of drag, the block fuel of *optimized_mod* was reduced by 3.6 percent.

In the present MDO system, surface spline function of the geometry deviation ΔZ was used for the modification of the wing shape (surface mesh) then the volume mesh was modified by the unstructured dynamic mesh method. However, this process made the surface mesh distorted around the leading edge and highly limited the design space shown in Fig. 38. This mesh generation process might be the primary reason for the difficulty in finding the non-gull geometry with better block fuel performance. The secondary reason is that only the small number of the generations has been performed. However, this result reveals that Data Mining technique salvages the information. It is demonstrated that the knowledge discovery by Data Mining regarding design space is an important aspect in the practical optimization.

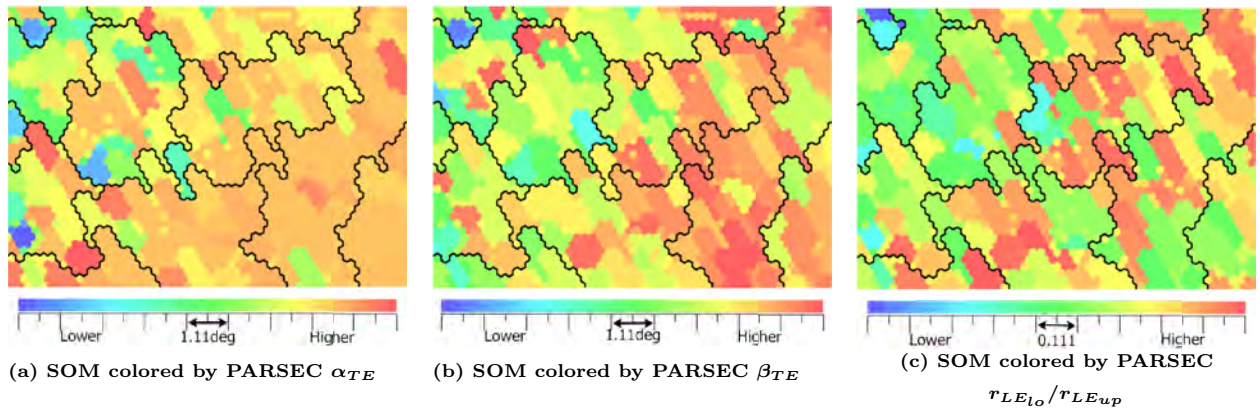


Figure 31. SOM colored by characteristic design variables regarding the PARSEC airfoil at 35.0% spanwise location. The minimum and maximum values of color bar are set using the minimum and maximum values of each design variable in optimizer, respectively.

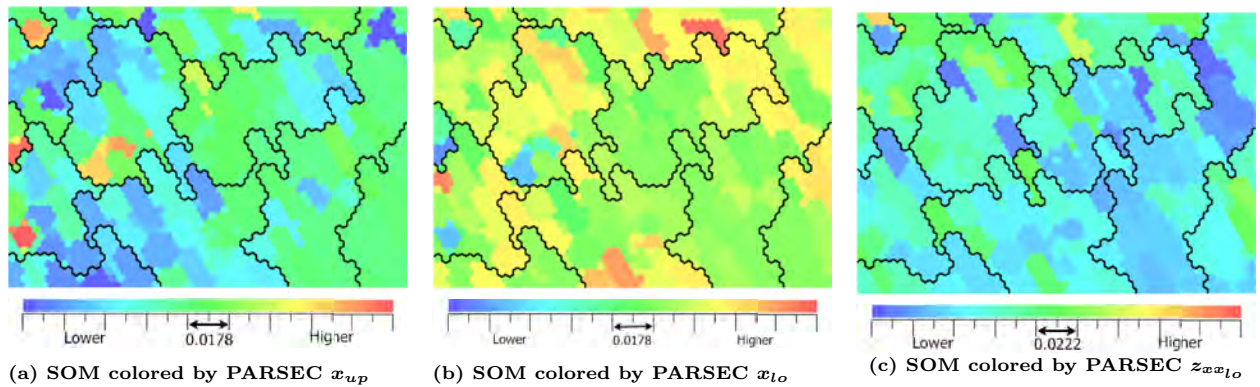


Figure 32. SOM colored by the characteristic design variables regarding the PARSEC airfoil at 55.5% spanwise location. The minimum and maximum values of color bar are set using the minimum and maximum values of each design variable in optimizer, respectively.

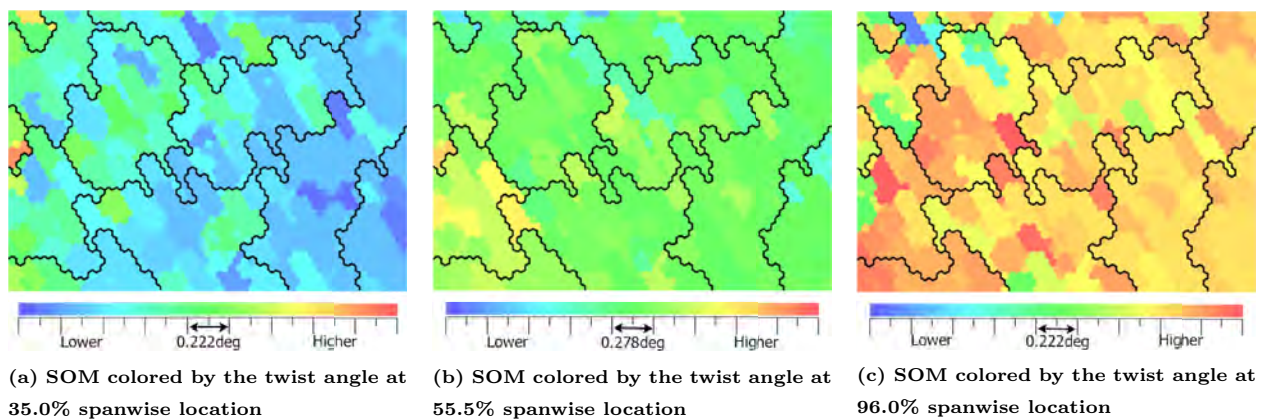


Figure 33. SOM colored by the characteristic design variables involving wing twist. The minimum and maximum values of color bar are set using the minimum and maximum values of each design variable in optimizer, respectively.

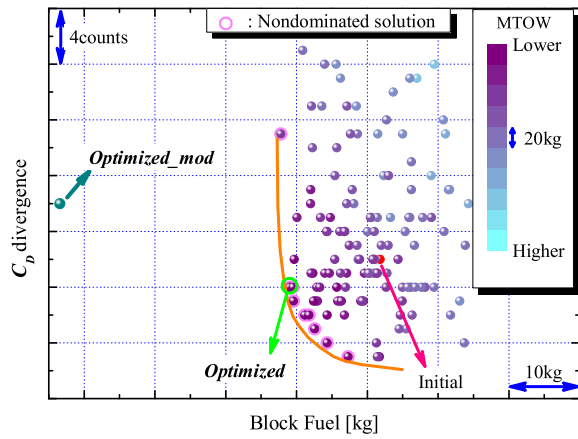


Figure 34. Comparison of *optimized_mod* and all solutions on two-dimensional plane between block fuel and C_D divergence.

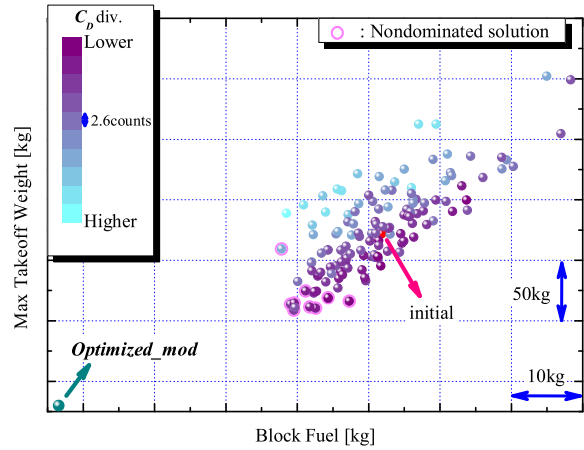


Figure 35. Comparison of *optimized_mod* and all solutions on two-dimensional plane between block fuel and maximum takeoff weight.

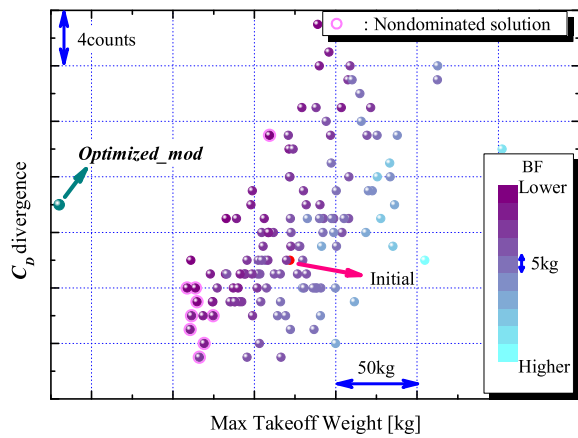


Figure 36. Comparison of *optimized_mod* and all solutions on two-dimensional plane between maximum takeoff weight and C_D divergence.

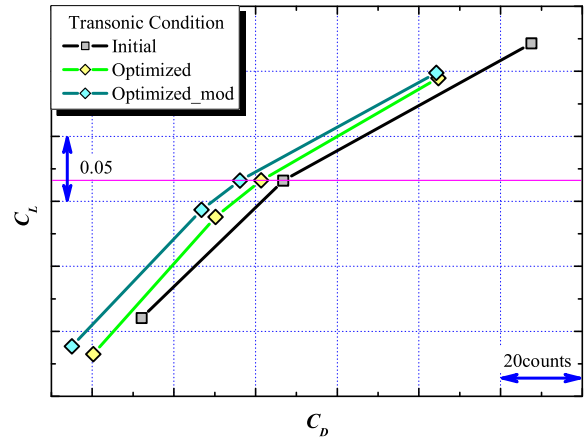


Figure 37. Comparison of the C_L - C_D curves among three geometries as initial, *optimized*, and *optimized_mod* under transonic flight condition.

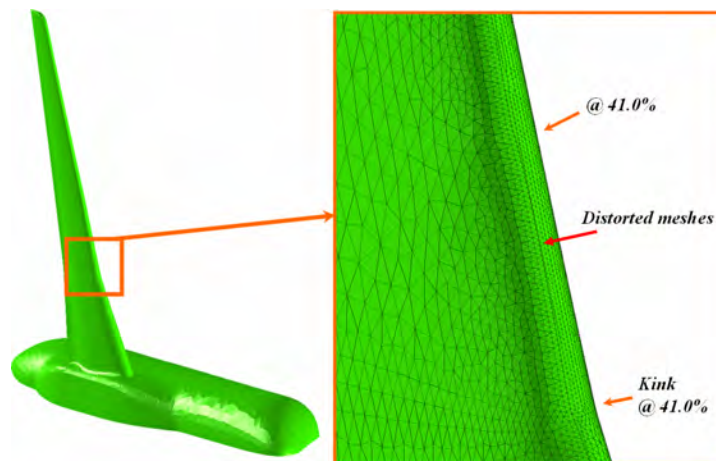


Figure 38. Example of distorted mesh in the vicinity of leading edge.

V. Conclusion

The wing shape of a regional jet aircraft was optimized using ARMOGA considering three aerostructural objective functions with high-fidelity evaluations. Consequently, the objective function value considering block fuel was reduced by over one percent as compared with the initial geometry. The geometry change in the vicinity of the kink was found to be effective for drag reduction. The tradeoff information among the three objective functions was revealed, and a main tradeoff was found between the block fuel and the drag divergence.

Moreover, Data Mining for the design space was performed using a Self-Organizing Map. As a result, particular design variables effective to improve the objective functions and aerodynamic performance were found. Detailed observations of SOM revealed that there is a sweet spot in the design space where the three objectives become relatively low.

One of the key features found by Data Mining was the non-gull wing geometry, although the present MDO results showed the inverted gull-wings as non-dominated solutions. When this knowledge was applied to one optimum solution, the resulting design was found to have better performance and to achieve 3.6 percent improvement in the block fuel compared to the original geometry designed in the conventional manner. The Data Mining technique provides knowledge regarding the design space and may salvage lost information during the optimization operation, which will be an important facet of solving practical optimization problems.

Acknowledgements

We would like to thank Dr. Oyama, A., research associate of Institute of Space and Astronautical Science, Japan Aerospace Exploration Agency for generating PARSEC geometry. We would also like to thank Mr. Takano, Y. and Mr. Kumano, T., graduate students of Tohoku University for generating the CATIA STL and the mesh data of the initial geometry, and the *optimized_mod* geometry, respectively. The Euler/Navier-Stokes computations were performed using NEC SX-5 in the Institute of Fluid Science, Tohoku University, and NEC SX-7 in Super-Computing System Information Synergy Center, Tohoku University.

References

- ¹Kroo, I., Altus, S., Braun, R., Gage, P., and Sobieski, I., "Multidisciplinary Optimization Methods for Aircraft Preliminary Design," AIAA Paper 94-4325-CP, 1994.
- ²Sobieszcanski-Sobieski, J. and Haftka, R. T., "Multidisciplinary Aerospace Design Optimization: Survey of Recent Developments," *Structural Optimization*, Vol. 14, No. 1, 1997, pp. 1–23.
- ³Martins, J. R. R. A., Alonso, J. J., and Reuther, J. J., "High-Fidelity Aerostructural Design Optimization of a Supersonic Business Jet," *Journal of Aircraft*, Vol. 41, No. 3, 2004, pp. 523–530.
- ⁴Oyama, A., Obayashi, S., Nakahashi, K., and Hirose, N., "Aerodynamic Wing Optimization via Evolutionary Algorithms Based on Structured Coding," *Computational Fluid Dynamics Journal*, Vol. 8, No. 4, 2000, pp. 570–577.
- ⁵Murayama, M., Nakahashi, K., and Matsushima, K., "Unstructured Dynamic Mesh for Large Movement and Deformation," AIAA Paper 2002-0122, 2002.
- ⁶Yamazaki, W., Matsushima, K., and Nakahashi, K., "Aerodynamic Optimization of NEXST-1 SST Model at Near-Sonic Regime," AIAA Paper 2004-0034, 2004.
- ⁷Sasaki, D., Obayashi, S., and Nakahashi, K., "Navier-Stokes Optimization of Supersonic Wings with Four Objectives Using Evolutionary Algorithm," *Journal of Aircraft*, Vol. 39, No. 4, 2002, pp. 621–629.
- ⁸Krishnakumar, K., "Micro-Genetic Algorithms for Stationar and Non-Stationary Function Optimization," *SPIE 1196, Proceedings of Intelligent Control and Adaptive Systems*, 1989, pp. 289–296.
- ⁹Fonseca, C. M. and Fleming, P. J., "Genetic Algorithms for Multiobjective Optimization: Formulation, Discussion and Generalization," *Proceedings of the Fifth International Conference on Genetic Algorithms*, 1993, pp. 416–423.
- ¹⁰Obayashi, S., Takahashi, S., and Takeguchi, Y., "Niching and Elitist Models for MOGAs, Parallel Problem Solving from Nature," *PPSN V, Lecture Notes in Computer Science*, Springer, Berlin, Heidelberg, New York, 1998, pp. 260–269.
- ¹¹Baker, J. E., "Reducing Bias and Inefficiency in the Selection Algorithm," *Proceedings of the Second International Conference on Genetic Algorithms*, 1987, pp. 14–21.
- ¹²Eshelman, L. J. and Schaffer, J. D., "Real-Coded Genetic Algorithms and Interval Schemata," *Foundations of Genetic Algorithms 2*, Morgan Kaufmann, San Mateo, CA, 1993, pp. 187–202.
- ¹³Deb, K., *Multi-Objective Optimization Using Evolutionary Algorithms*, John Wiley & Sons, Ltd., Chichester, 2001.
- ¹⁴"MSC. website," URL: <http://www.mscsoftware.com/> [cited 14 September 2004].
- ¹⁵Ito, Y. and Nakahashi, K., "Direct Surface Triangulation Using Stereolithography Data," *AIAA Journal*, Vol. 40, No. 3, 2002, pp. 490–496.
- ¹⁶Sharov, D. and Nakahashi, K., "A Boundary Recovery Algorithm for Delaunay Tetrahedral Meshing," *Proceedings of the 5th International Conference on Numerical Grid Generation in Computational Field Simulations*, 1996, pp. 229–238.

- ¹⁷Ito, Y. and Nakahashi, K., "Improvements in the Reliability and Quality of Unstructured Hybrid Mesh Generation," *International Journal for Numerical Methods in Fluids*, Vol. 45, Issue 1, 2004, pp. 79–108.
- ¹⁸Obayashi, S. and Guruswamy, G. P., "Convergence Acceleration of an Aeroelastic Navier-Stokes Solver," *AIAA Journal*, Vol. 33, No. 6, 1994, pp. 1134–1141.
- ¹⁹Venkatakrishnan, V., "On the Accuracy of Limiters and Convergence to Steady State Solutions," AIAA Paper 93-0880, 1993.
- ²⁰Sharov, D. and Nakahashi, K., "Reordering of Hybrid Unstructured Grids for Lower-Upper Symmetric Gauss-Seidel Computations," *AIAA Journal*, Vol. 36, No. 3, 1998, pp. 484–486.
- ²¹Dacles-Mariani, J., Zilliac, G. G., Chow, J. S., and Bradshaw, P., "Numerical/Experimental Study of a Wingtip Vortex in the Near Field," *AIAA Journal*, Vol. 33, No. 9, 1995, pp. 1561–1568.
- ²²Chiba, K., Obayashi, S., and Nakahashi, K., "CFD Visualization of Second Primary Vortex Structure on a 65-Degree Delta Wing," AIAA Paper 2004-1231, 2004.
- ²³Yamazaki, W., "Aerodynamic Optimization of Near-Sonic Plane Based on NEXST-1 SST Model," ICAS 2004-4.3.4, 2004.
- ²⁴Kohonen, T., *Self-Organizing Maps*, Springer, Berlin, Heidelberg, 1995.
- ²⁵"Eudaptics website," URL: <http://www.eudaptics.com> [cited 16 June 2004].
- ²⁶Deboeck, G. and Kohonen, T., *Visual Explorations in Finance with Self-Organizing Maps*, London, Springer Finance, 1998.
- ²⁷Vesanto, J. and Alhoniemi, E., "Clustering of the Self-Organizing Map," *IEEE Transactions on Neural Networks*, Vol. 11, No. 3, 2000, pp. 586–600.